Comparison of nanocomposite dispersion and distribution for several melt mixers

Danielle Veigel [a,b], Kabir Rishi [a,c], Ugochukwu Okoli [a], Gregory Beaucage [a,*], Jeffrey A. Galloway [b], Hannah Campanelli [a,b], Jan Ilavsky [d], Ivan Kuzmenko [d], Melodie Fickenscher [e]

[a] Chemical & Materials Engineering, University of Cincinnati, Cincinnati, OH, 45221, USA
[b] KraussMaffei, Florence, KY, 41042, USA
[c] Centers for Disease Control and Prevention, National Institute for Occupational Safety and Health, Cincinnati, OH, 45213, USA
[d] X-Ray Science Division, Advanced Photon Source, Argonne National Laboratory, Lemont, IL, 60439, USA
[e] Advanced Materials Characterization Center, College of Engineering & Applied Sciences, University of Cincinnati, Cincinnati, OH, 45221, USA

ARTICLE INFO

ABSTRACT

Breakup (dispersion) and distribution of nanoparticles are the chief hurdles towards taking advantage of nanoparticles in polymer nanocomposites for reinforcement, flame retardancy, conductivity, chromaticity, and other properties. Microscopy is often used to quantify mixing, but it has a limited field of view, does not average over bulk samples, and fails to address nano-particle hierarchical structures. Ultra-small-angle X-ray scattering (USAXS) can provide a macroscopic statistical average of nanoscale dispersion (breakup) and emergent hierarchical structure, as well as the distribution on the nanoscale. This work compares several common mixer geometries for carbon black-polystyrene nanocomposites. Two twin-screw extruder geometries, typical for industrial processing of melt blends, are compared with a laboratory-scale single screw extruder and a Banbury mixer. It is found that for a given mixer, nanoscale distribution increases following a van der Waals function using accumulated strain as an analogue for temperature while macroscopic distribution/dispersion, using microscopy, does not follow this dependency. Breakup and aggregation in dispersive mixing follow expected behavior on the nanoscale. Across these drastically different mixing geometries an unexpected dependency is observed for nanoscale distributive mixing (both nano and macroscopic) as a function of accumulated strain that may reflect a transition from distributive turbulent to dispersive laminar mixing as the mixing gap is reduced.

1. Introduction

Melt processing for nanocomposites relies heavily on optimal nanofiller distribution and dispersion (particle breakup). Determination of processing parameters that impart the most favorable properties is ever evolving. There are five main methods to melt process nanocomposites: calendering, Banbury mixing, single-screw extrusion, co-rotating twin-screw extrusion, and counter-rotating twin-screw extrusion [1]. In industrial grade twin-screw extruders, the screws can be customized to best suit a nanocomposite filler and its desired properties. For fillers like carbon black, the nanoparticle dispersion (breakup/aggregation/agglomeration) and distribution within the products can vastly alter their properties. In polymer processing a distinction is made between the breakup of granules/pellets, dispersive mixing, and the re-distribution of particles, distributive mixing [1]. In addition to

these distinctions, for materials such as carbon black, the size-scale hierarchy of mixing must be considered since macroscopic mixing can significantly differ from nano-scale mixing. For example, silica easily mixes with organic elastomers on a macroscopic scale but can form nano-scale clusters that reduce the desired nano-composite properties. Macrodispersion assesses the incomplete breakup of filler pellets into agglomerates (1 μm to >100 μm in size) through tensile strength distribution and optical microscopy. These large inclusions/flaws decrease the tensile strength of the composite based on Griffith-Orowan-Irwin theory of fracture [2–4], though these imaging techniques are semi-quantitative. Conversely, microdispersion is associated with filler aggregation/networking on the nano-to micron size scales and can be detected by the rheological Payne effect and ultra-small angle X-ray scattering (USAXS). USAXS can directly quantify breakup, aggregation and agglomeration on the nano-to micro-scales from an average over

macroscopic scales that evaluates dispersive mixing. Simultaneously, USAXS can be used to quantify the second-virial coefficient and the associated interaction potentials [5–7] which describes distributive mixing. In this study the nanodispersion/distribution of carbon black in melt compounded polymers is compared for several extruders/mixers, screw designs, and screw speeds. The USAXS nano-scale method is compared with a macroscopic imaging method.

1.1. Extrusion systems for polymer compounding

Three mixers were utilized in this paper: a Banbury mixer, a single-screw extruder (SSE), and a co-rotating twin-screw extruder (TSE). Banbury mixers are internal batch mixers with counter-rotating mixing blades. They are typically used for highly filled compounds (concentrates); the product later being fed and processed by an extruder [8]. Single-screw extruders are popular for their reliability and cost-effectiveness. They excel at building pressure and are largely used for thermoplastic elastomers and PVC. When specialized mixing is the most important aspect of the process, twin-screw extruders may be preferred due to their intermeshed screws and versatility. While there are different rotors and screws available for both the Banbury and SSEs, industrial grade TSEs are built element by element like a shish-kebab. This ensures that the screws can be customized to achieve ideal melt and mix quality.

Accumulated strain can be a measure of the driving force for convective mixing just as temperature drives diffusive mixing [5]. For batch mixers, like the Banbury mixer, the accumulated strain is proportional to the mixing speed times the residence time. For extruders, the mixing speed and residence time are coupled since the barrel is of fixed length. For a simple, model screw that is filled completely, faster screw rotation results in a proportional reduction in the residence time resulting in no change in the accumulated strain. For complex screws where the barrel is not completely and not uniformly filled, Fig. 1(d), increasing the extrusion speed changes the distribution of melt in the various segments leading to a change in accumulated strain. A further complication is that little distributive mixing occurs in laminar mixing at low Reynolds numbers for narrow flow gaps while extensive distributive mixing occurs in turbulent flow at high Reynolds numbers with wide flow gaps. We have found that regardless of the flow geometry and laminar/turbulent mix in a complex mixer, an increase in accumulated strain leads to better mixing for that one geometry [6,7]. However, when comparing different mixing geometries, where higher accumulated strain is associated with narrower flow gaps, the proportional transition from turbulent to laminar flow has the opposite impact on distributive mixing, i.e., a reduction in distributive mixing with greater accumulated strain associated with narrow flow gaps as demonstrated below.

TSEs typically contain feed, melting, side feed, mixing, venting, and pressure building sections before the samples are processed into the final product as depicted in Fig. 1(d) [9]. SSEs have three geometrically different sections, but only one pressure building section. The three sections in SSEs include the feed section, the metering section, and the compression section [10]. In a Banbury mixer and single-screw extruder the mixing chamber is typically filled to 70% since they are bulk fed as shown in Fig. 1(a) and (b), respectively. In a twin-screw extruder, only a fraction of the mixing chamber is filled because it is starve-fed with a constant feed rate as shown in Fig. 1(c) where the black granular material is the compound being mixed and the white area is open space. In Fig. 1(d) the blue area contains the polymer compound.

A screw is described by the pitch, which is the length in screw outer diameters of a full turn of the thread, so the pitch is proportional to the sine of the angle of the thread along the screw. The feeding section of a twin-screw extruder contains forward conveying elements with a longer pitch to introduce the material, Fig. 1(d). The pitch of the conveying elements is then reduced to increase the fill level in the extruder as the material progresses to the melt section. The melt section can vary in length and aggression through the selection of different mixing elements and can be tuned for materials with different melt flow indices (viscosities). For example, forward kneading elements, Fig. 2, with narrow discs can introduce the material to the melt section, followed by forward kneading elements with wider discs. Wider discs allow more material to pass between the tips of the kneading elements and the barrel walls, creating higher shear and more dispersive mixing (particulate breakup). Thinner disks force more material between kneading elements, splitting the flow and creating more distributive mixing (particle organization). Reverse conveying elements or neutral kneading elements can be used to build pressure and increase the fill level, if necessary, as shown in Fig. 1 (d). If a side feeder is being used to incorporate filler, forward conveying elements with long pitches will be used to lower the degree of fill to prevent material from overflowing (flooding) out of the feeder vents.

Mixing sections can vary depending on the filler bulk density, filler type, and desired final properties. Low density fillers convey air into the melt, and elements that are axially open allow the air to vent either up- or downstream. Forward conveying kneading elements with wide disks are more aggressive than those with narrower disks, shown in Fig. 2(a).
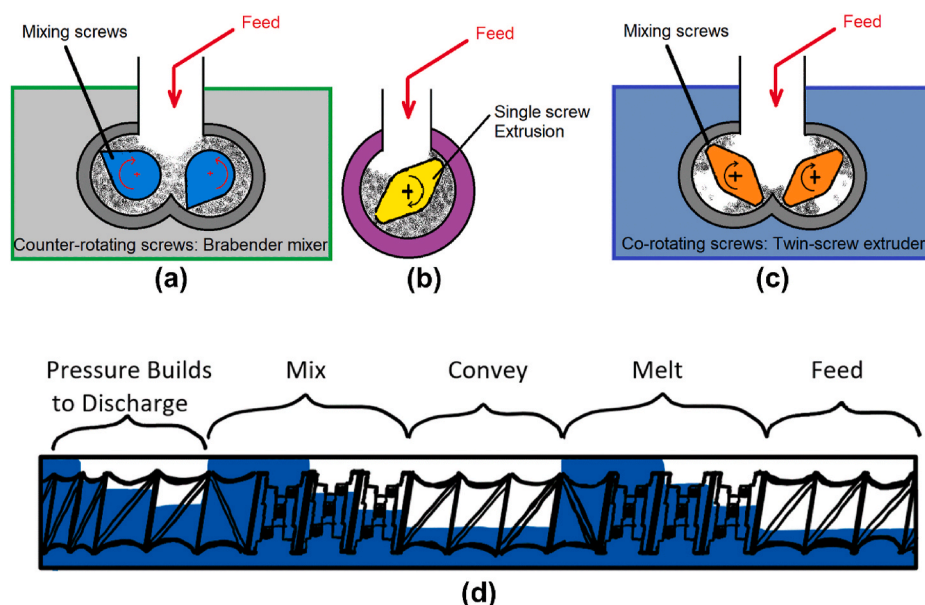
Fig. 1. Cross-section of three mixers. (a) Banbury mixer, (b) Single-screw extruder, and (c) Twin-screw extruder, showing the melt flow channels (d) Axial sketch of a twin-screw extruder showing general elements and fill levels within the feed, melt, mixing, and pressure building sections. Grey granular regions in (a), (b) and (c) are the polymer compound as is the blue region in (d). (For interpretation of the references to color in this figure legend, the reader is referred to the Web version of this article.)
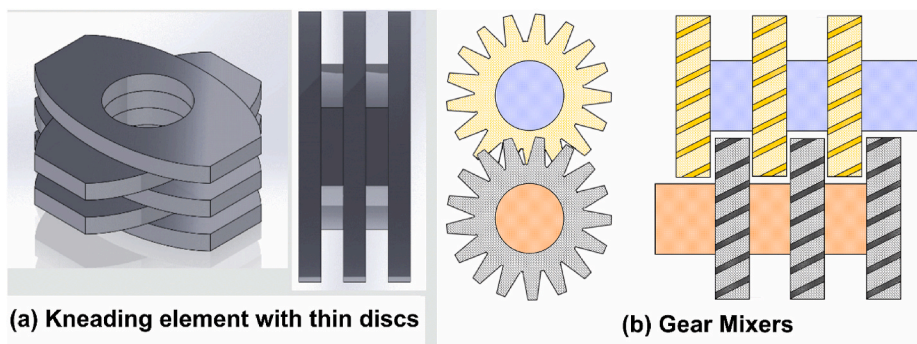
Fig. 2. (a) 90° kneading elements for twin screw extruders; (b) Gear mixers for twin screw extruder.

For more distributive mixing, forward kneading elements with narrow disks can be used with or without gear mixers, shown in Fig. 2(b). The venting zone follows the mixing zone, requiring forward conveying elements with longer pitch. Longer pitch increases the volume threshold and reduces the degree-of-fill, lowering the chance of vent flooding and increasing the volume of material that can pass through those sections. Vacuum vents require melt seals upstream and downstream to prevent the pressure from affecting other zones. Melt seals can be achieved, for example, via neutral kneading elements and reverse conveying elements. Finally, the pressure building zone allows the material to achieve enough pressure to be passed through the final processing unit, usually a die of some kind. The pressure building section needs to be long enough to prevent flooding into any vents and usually consists of forward conveying elements of consistently reducing pitch to increase fill level and pressure.

1.2. Measuring nano-dispersion

Current methods to measure dispersion include residence stress distribution (RSD) [11,12], photoluminescent spectroscopy [13,14], analysis of micrographs [15], transmission and scanning electron microscopy (TEM, SEM). RSD is a method of measuring stress in extruders, combining stress distribution history and residence time distribution (RTD). It utilizes calibrated microencapsulated sensor (CAMES) beads and dyed beads that rupture at certain stresses, to create a profile of how much material receives a designated amount of stress along the RTD [11, 12]. We argue that the quantification of dispersion is size specific. For example, optical methods and scanning electron microscopy can only describe two orders in size. Transmission electron microscopy could cover a much smaller size adding another two orders of magnitude on the nanoscale. Other than the extensive sample preparation, the 100 nm thick cryotome sections reveal only a local state of dispersion in TEM. Sampling of heterogeneous materials is poor for microscopic techniques due to the limited field of view. Moreover, traditional microscopic information is a two-dimensional projection of 3D space thereby limiting a detailed, quantitative understanding of the 3D filler distribution and its hierarchy. More recent work that uses tomography to reconstruct three-dimensional structures of polymeric nanocomposites is limited to the micron-scale [16]. Typically, nanofillers are incorporated to enhance bulk conductivity, UV absorption, and improve the static and dynamic response. Each purpose favors different levels of structure in the filler's multi-hierarchy [17] and subsequent extent of dispersion at that level. For example, the frequency dependent dynamic response of a carbon black nanocomposites is linked to their nanoscale networks, whereas the bulk conductivity depends on their micron-scale networks [18]. These analytic challenges can be overcome by using combined small-angle scattering techniques such as SAXS and USAXS that extend the spatial resolution from μm to Å i.e., about four decades in size. Additionally, SAXS/USAXS measurements are made over macroscopic dimensions resulting in a bulk average measure of the nanoscale

structure, its hierarchical dispersion and size-dependent distribution.

1.2.1. Dispersive mixing/monitoring the change in nanoaggregate structure

As opposed to microscopy which involves a direct imaging of space, most interpretation and analysis of small-angle scattering (SAXS) data occurs in reciprocal space which is a Fourier transform of the real space. Analysis of SAXS data usually involves model fits to the reduced scattering intensity, $I_0(q)/\phi_0$. One universal model, the Unified fit [19], combines all the structural levels in the filler hierarchy and presents information about the size, structure, surface area to volume ratio and the number density of the particles. The size as measured by the radius of gyration, the number density and volume of the particles at each structural level is based on Guinier's law [20] whereas, the morphology and the surface area to volume ratio is based on Porod's and other power-laws [21]. The Unified Function [19] is derived as:

$$\frac{I_0(q)}{\phi_0} = \sum_{i=1}^{n} \left[\frac{G_i}{\phi_0} \exp\left(-\frac{q^2 R_{g,i}^2}{3} \right) + \frac{B_i}{\phi_0} (q_i^*)^{-P_i} \exp\left(-\frac{q^2 R_{g,i-1}^2}{3} \right) \right] \quad (1)$$

where, the subscript "*i*" reflects the index of the structural level that is generally numbered from the smallest size-scale (primary particles, $i = 1$) to the larger size-scales (aggregates, $i = 2$); $q_i^* = q / [\mathrm{erf}(kqR_{g,i}/\sqrt{6})]^3$ and "erf" is the error function [19]. k has a value of 1 for $P_i > 3$ and a value of 1.06 is generally used for $P_i < 3$. $R_{g,0} = 0$ indicates no high-q cutoff or termination to the level 1 Porod power-law decay. Each structural level in the Unified Function in equation (1) involves four generic parameters, the Guinier prefactor, G_i, that is related to the electron density, volume and number density of particles at that level, the radius of gyration, $R_{g,i}$, the power-law prefactor, B_i, that is related to the surface area to volume ratio (S/V), and the power-law slope, P_i, that is related to the particle morphology at that level. Note that the units of $I_0(q)/\phi_0$ on the absolute scale is cm^{-1} since it represents the differential scattering cross-section normalized by the irradiated volume. A schematic of the primary particle and aggregate structure levels as observed in USAXS for typical carbon blacks is shown in Fig. 3. Notice that the primary particles are made of elementals that are not typically observed in scattering, although they can be resolved through electron microscopy as proposed by Koga et al. [17,22,23]. These elementals comprise of graphitic layers that display a power law scaling of −2 in scattering.

As previously discussed, processing of nanocomposites results in dispersive fracture of the filler agglomerates to ~100 nm aggregates that are made up of primary particles. To assess dispersion on these size scales, we limit the index "*i*" in equations (1) and (2), thereby reducing equation (1) to the first two structural levels. Industrial nanoaggregates are branched mass-fractals. The mass-fractal dimension, d_f, equals the negative of the power-law slope for level 2, P_2, from the fit in equation (1). To estimate the extent of dispersive mixing (agglomerate breakup), the aggregate topology specified by parameters derived from the fit parameters in equation (1), can be used. These topological parameters are: the size of primary particle as the Sauter mean diameter, $d_p = 6 \, V/S$;
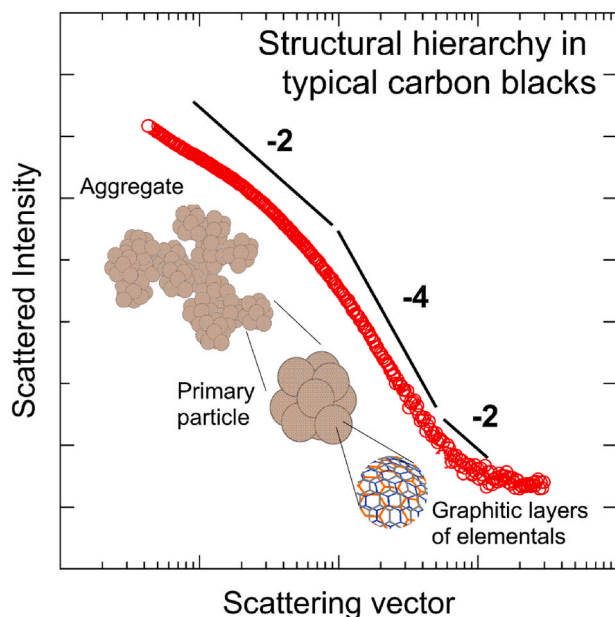
Fig. 3. Typical X-ray scattering profile as a function of scattering vector for carbon black that displays characteristic power law scaling of −2, about −4, and about −2 (right to left) that correspond to graphitic layers on elementals, primary particles, and aggregates, respectively. Note that the elementals are clustered together into 3D primary particles whereas the primary particles are aggregated into mass fractals. A schematic of the different structural levels adapted with permission from T. Koga, T. Hashimoto, M. Takenaka, K. Aizawa, N. Amino, M. Nakamura, D. Yamaguchi, S. Koizumi, New insight into hierarchical structures of carbon black dispersed in polymer matrices: A combined small-angle scattering study, Macromolecules. 41 (2008) 453–464. Copyright © 2008 American Chemical Society, is also shown.

the degree of aggregation or the average number of primary particles in an aggregate, $z = (G_2/G_1) + 1$; the aggregate end-to-end distance, $R_{eted} = d_p(z)^{1/df}$; the aggregate tortuosity dimension, $d_{min} = (B_2 R_{g,2}^{df}) / (C_p \Gamma(d_f/2) G_2)$, where, C_p represents the aggregate polydispersity close to M_z/M_w [24,25]; the short circuit path, $p = (R_{eted}/d_p)^{dmin}$; the aggregate connectivity or topological dimension, $c = d_f/d_{min}$; and the branch fraction, $\phi_{br} = (z\text{-}p)/z$ [26–29]. Note that there is a good correlation between the d_p obtained from X-ray scattering studies and BET measurements [30].

1.2.2. Distributive (organizational) mixing/measuring the nanoaggregate interaction parameter

Changes to the aggregate topology, as described above, can only be determined when the filler concentration in the nanocomposite is sufficiently dilute (ϕ_0) such that there is no overlap of neighboring nanoaggregates which obscure structures larger than the structural screening length. Practically, such dilute conditions are seldom seen commercially and at higher loadings (semi-dilute, ϕ) aggregate interactions can be observed. This is reflected by a diminishment in the reduced scattering intensity, $I(q)/\phi$ as compared to $I_0(q)/\phi_0$ at low-q (large size), called structural screening [5]. In the limit of $q \to 0$, the extent of structural screening due to particle-particle interactions, ν, for different nanofiller loadings can be quantified through the random phase approximation (RPA) equation of deGennes and Edwards,

$$\frac{\phi}{I(q=0)} = \frac{\phi_0}{I_0(q=0)} + \phi\nu \tag{2}$$

if a mean-field assumption is made [7,31–33]. A mean-field assumption is reasonable in the absence of specific interactions that occur with charged aggregates like silica [34]. Note that ν (cm) is an effective interaction parameter for all the particles in the system and reduces the

many-body problem to a single mean-field. Equation (2) can be rewritten in terms of the scattering structure factor [34],

$$S(q) = \frac{I(q)/\phi}{I_0(q)/\phi_0} = \frac{1}{1 + \phi\nu\{I_0(q)/\phi_0\}} \tag{3}$$

"ν", measured at $q \to 0$ is proportional to the binary interaction parameter, A_2, as shown by Vogtt et al. [33] who used the Pedersen and Sommer formalism [32] to study worm-like micelles,

$$A_2 = \nu\langle\Delta\rho^2\rangle \big/ 2N_A(\rho_f)^2 \tag{4}$$

,such that $<\Delta\rho^2>$ represents the squared difference in the scattering length densities of the nanofiller and the polymer matrix or the electron contrast (cm^{-4}), N_A is Avogadro's number and ρ_f is the nanofiller density in g/cm^3. A_2 (mol cm^3/g^2) is a measure of the extent of distributive (organizational) mixing. A_2 is positive for high degrees of distribution, negative for phase separation, clustering, or flocculation and 0 for the limit of separation/clustering, in the case of melt mixing of polymers this can be the wetting time [6,7] if mixing is observed as a function of residence time. To determine how the binary interaction parameter, ν, varies with mixing conditions, Rishi et al. [7] considered a thermal analogy. It is well known that the temperature dependence of the second virial coefficient, $B_2 = A_2 (M^2/N_A)$, can be expressed through the van der Waals (vdW) equation of state, where $M = \rho_f N_A z (\pi d_p^3/6)$ represents the nanoaggregate mass (g/mol). In viscous polymeric media, the distribution of immiscible nanoparticles is dictated by the accumulated strain imparted during the high shear mixing process as opposed to temperature in a thermally equilibrated system [6,34]. Considering the accumulated strain, γ_{acc}, as analogous to thermal energy, k_BT, allows for quantification of dispersion in terms of the excluded volume of the fractal aggregates, b^*, and the attractive interaction potential between aggregates that lead to segregation, a^*, from the van der Waals formalism where "*" indicates that this is an approximation based on an analogy between thermal distribution by Brownian motion and kinetic distribution by accumulated shear strain,

$$B_2{}^* = b^* - (a^* / \gamma_{acc}) \tag{5}$$

B_2^* can often be directly calculated from the dilute scattering curve if bound polymer can be ignored (b^* can also be used to measure the extend of bound polymer) [7,34]. B_2^* has units of cm^3/aggregate [5]. In equation (5), the accumulated strain, γ_{acc}, accounts for the mixing geometry, Ψ, the residence time, t_{res} (min or s), and the rotational speed, $\dot{N}$ (rpm) such that, $\gamma_{acc} = \Psi\dot{N}t = \dot{\gamma}t$ since the strain rate, $\dot{\gamma} = \Psi\dot{N}$ for equations (6) and (7) as shown below.

1.2.2.1. Estimation of the accumulated strain for the Banbury mixer.
For a Banbury mixer, the geometry can be described between the rotor with diameter, D_R, and the concentric wall with diameter D_W using Couette flow [35,36], such that the accumulated strain at the wall can be approximated as,

$$\gamma_{acc,M} = \dot{\gamma}t_{res} = \left(\frac{4\pi}{n\{(D_W/D_R)^{2/n} - 1\}}\right)\dot{N}t_{res} \tag{6}$$

In equation (6), $\dot{N}$ (rpm) is the rotational speed, n represents the power-law index for shear thinning viscosity and is approximately equal to 0.28 for polystyrene (the polymer used here) at 170 °C [37]. Note that t_{res} for a batch mixer equals the mixing duration. For continuous mixers such as extruders, t_{res} and $\dot{N}$ are inversely related.

1.2.2.2. Estimation of the accumulated strain for single screw extruder.
For a single screw extruder, the accumulated strain can be estimated through the barrel diameter, D_W, and the channel depth or screw-barrel gap, $h(L)$ which is a function of the screw length, L [38], such that,

$$\gamma_{\text{acc,SSE}} = \dot{\gamma} t_{\text{res}} = \left(\frac{\pi \{ D_{\text{W}} - 2h(L) \}}{h(L)} \right) \dot{N} t_{\text{res}} \tag{7}$$

The average residence time, t_{res} (min), for the single screw extruder was estimated from the ratio of the free volume, $V_{\text{free}} = V_{\text{barrel}} + V_{\text{die}} - V_{\text{shaft}} - n_{\text{flight}} V_{\text{flight}}$, to the volumetric flow rate, $\dot{Q}$, measured in cm^3/min if a 100% conveying efficiency is assumed, as opposed tracer methods used to determine the residence time distribution [39,40]. Here, $\dot{N}$ represents the screw speed measured in rpm. Notice that in equation (7), the residence time, t_{res} accounts for the viscoelastic behavior of the polymer melt since a material with lower melt flow index will have a longer residence time. The barrel volume, $V_{\text{barrel}} = \pi \left(\frac{D_{\text{w}}}{2} \right)^2 L$, whereas the die volume, $V_{\text{die}} = \pi \left(\frac{D_{\text{bore}}}{2} \right)^2 L_{\text{bore}}$. Note that since the screws in an SSE are generally tapered the volume of the screw shaft, $V_{\text{ss}} = \frac{\pi}{3} \left\{ \left(\frac{D_{\text{ss}}^{\text{max}}}{2} \right)^2 + \left(\frac{D_{\text{ss}}^{\text{max}} D_{\text{ss}}^{\text{min}}}{4} \right) + \left(\frac{D_{\text{ss}}^{\text{min}}}{2} \right)^2 \right\} L$. The volume of a screw flight, $V_{\text{flight}} = \pi \left(\frac{D_{\text{flight}}}{2} \right)^2 L_{\text{flight}}$.

1.2.2.3. Estimation of the accumulated strain for twin-screw extruder. The above estimates might reasonably approximate the accumulated strain in small-scale laboratory mixers and extruders, however, for large-scale industrial extruders these approximations are insufficient. Industrial grade twin-screw extruders are "starvation-fed," limited at the low feed end by an empty mixing chamber and surging of the polymer melt and at the high feed end by filling of the mixing chamber, with torque and heating. Because twin-screw extruders are starvation fed and do not continuously run full, precise computations of $\gamma_{\text{acc,TSE}}$ depends upon the degree-of-fill or the extruder free volume. The addition of intermeshing screws adds another degree of complexity, making calculations difficult.

The accumulated strain for TSEs can be estimated by summing over the average strains due to each screw element, $\gamma_{\text{acc,TSE}} = \sum \gamma_{\text{acc}}$. Although the polymer melt flow within the TSE is complex, $\gamma_{\text{acc,TSE}}$ can be approximated if two assumptions can be made: (a) each flow channel contains the same amount of material; and (b) the difference in strain experienced by the material in the intermeshing region of the screws is negligible. These simplifications allow the accumulated strain to be estimated from only one melt flow channel within the screws.

To calculate the accumulated strain, γ_{acc}, for a screw element, both the residence time, t_{res} (s), and average shear rate, $\dot{\gamma}_{\text{avg}}$ (s^{-1}), are needed such that,

$$\gamma_{\text{acc}} = \dot{\gamma}_{\text{avg}} t_{\text{res}} \tag{8}$$

The estimation of t_{res} depends on whether the geometry of the screw element builds pressure during melt flow or not. Elements with an effectively reversed or neutral conveying geometry enhance pressure, while elements with forward conveying geometry do not. The residence time for elements that do not pressurize the melt can be determined from,

$$t_{\text{res,np}} = 60l / \psi \dot{N} \zeta \tag{9}$$

$t_{\text{res,np}}$ depends on the extruder screw speed, $\dot{N}$ (rpm), the element's conveying efficiency, θ (%), the element's pitch, ζ, and length, l. The element's pitch and length are typically expressed in terms of the screw's outer diameter, D_0. Additionally, the conveying efficiency, θ, is largely due to the element's geometry and has been designated in prior work by Schuler [9]. On the contrary, the residence time for elements that build substantial pressure depends on the estimated fill level, Ω (%), the element free volume, V_{free} (cm^3), and the volumetric flow rate, $\dot{Q}$ (liters/hour) such that,

$$t_{\text{res,p}} = 3.6 \Omega V_{\text{free}} / \dot{Q} \tag{10}$$

$\Omega \approx 100\%$ for reverse or neutral elements that create a melt seal which requires pressure to be overcome. Additionally, the elements in the backup of the created melt seal will also have some pressure and the fill levels of those elements need to be estimated. The estimation of V_{free} from the element's geometry has been described by Schuler [9].

Estimation of the average shear rate is complicated since the screw-barrel gap, h (mm), depends on the screw geometry. During screw rotation, h changes relative to the tip and flank angle of the screw element. To calculate the average shear rate, $\dot{\gamma}_{\text{avg}}$ (s^{-1}), the element can be divided into sections based on the area traversed during rotation relative to the tip and flank angles as shown in Fig. 4. $\dot{\gamma}_{\text{avg}}$ can be determined summing the product of the shear rate for each section "i" of the screw element, $\dot{\gamma}_i$, and the area it encompasses, A_i (mm^2), normalized by the total area enclosed by all the sections,

$$\dot{\gamma}_{\text{avg}} = \sum \dot{\gamma}_i A_i / \sum A_i \tag{11}$$

$\dot{\gamma}_i$ depends on the extruder geometry, i.e., the outer diameter of the screw, D_0 (mm), the screw-barrel gap, h_i, and the screw speed, $\dot{N}$ (rpm), for that section of the screw element such that,

$$\dot{\gamma}_i = \pi D_o \dot{N} / 60 h_i \tag{12}$$

Notice that equation (12) is like equation (7) for the single-screw extruder. For the conveying or kneading elements, the screw-barrel gap can be calculated using equations derived by Schuler [9]. For other mixing elements such as specific gear mixers used in this study, the estimates of h_i are provided by KraussMaffei, Florence, KY 41042, USA.

In this study, the accumulated strain for laboratory and industrial grade polymer processing equipment with different mixing speeds and mixing geometries was computed. Although, the design of industrial grade twin-screw extruders is inherently more complex than laboratory grade mixers, the estimation of the mean accumulated strain serves as a good measure of the shear experienced by the nanofiller compounds. Carbon black distribution in these instruments was compared based on the second virial coefficient obtained from small-angle X-ray scattering
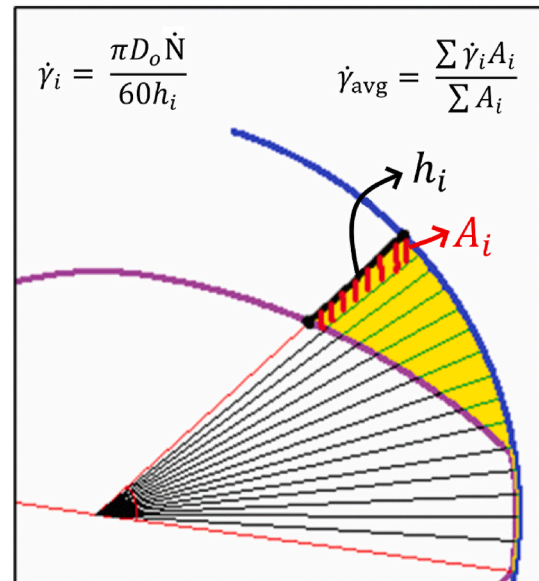
Fig. 4. An image depicting a portion of a conveying element. Below the blue line is the barrel. Below the purple line is the solid screw. The yellow area indicates the filled area of the screw element, $\sum A_i$, comprising of sections of area, A_i. The black lines separate the screw face into equidistant sections, and the green lines indicate the screw-barrel gap (h_i). The screw-barrel gap is used in the calculation of the shear rate ($\dot{\gamma}_i$) for each green line. The area to the clockwise side of the green line is used to determine the average shear rate for the element. (For interpretation of the references to color in this figure legend, the reader is referred to the Web version of this article.)

measurements.

2. Experimental

2.1. Sample preparation

Samples were prepared using a 50 g internal Brabender Plasticorder® mixer with counter rotating Banbury-type blades, a single-screw vertical microtruder from Randcastle Extrusion Systems, Inc. Cedar Grove, NJ 07009, and a ZE 28 BluePower twin-screw extruder with co-rotating screws from KraussMaffei, 7095 Industrial Rd, Florence, KY 41042, and Munich, Germany with two different screw designs. One screw design, intended for more distributive mixing, utilized gear mixers (GM) in the mixing section, while the other screw design, intended for more dispersive mixing, used 1.25D 45° and 90° forward conveying kneading blocks (KB). A 35% by weight carbon black (that conforms to ASTM grade N110)/polystyrene masterbatch from Modern Dispersions, Inc., 78 Marguerite Ave, Leominster, MA 01453 was processed with AmSty STYRON™ 666D [41] clear polystyrene with a melt-flow index of 8 g/10min at 200 °C. Note that the masterbatch was produced with the same grade of polystyrene, AmSty STYRON 666D. The amount of the two resins was controlled to produce samples with approximately 1%, 5%, 10%, 15%, and 20% by weight (φ_{wt}) of carbon black (dilute volume fraction, $\varphi_0 = 0.005$; semi-dilute volume fractions, φ, ranging from ~0.025 to ~0.12) on all processing equipment. The twin-screw extruder was run at 300 and 400 rpm, using both screw geometries. The samples were pelletized following extrusion. Each twin screw extruder sample is referred with letters to designate the screw design, GM (gear mixer) or KB (kneading block), followed by the screw speed (rpm) as shown in Table 1. The N110 grade is a high-structure carbon black with a specific surface area of 143 m²/g and a Sauter mean diameter (6 V/S) of ~23 nm [42].

Table 1 also lists the accumulated strain experienced by the filler particles for each processing geometry. For the Banbury mixer, $D_W = 40$ mm, $D_R = 28.5$ mm, $n = 0.28$ for polystyrene at 170 °C [37], and the mixing duration, t_{res} was 6 min. For the SSE barrel, $D_W = 12.7$ mm, $L = 343$ mm, whereas the channel depth, h ($L = 343$ mm) was 0.7 mm. For the die used on the SSE, $D_{bore} = 6.3$ mm whereas $L_{bore} = 45$ mm. The screw shaft diameter at the top (near the start of the feeding zone), $D_{ss}^{min} = 6.3$ mm while, at the bottom (at the end of the metering zone), $D_{ss}^{max} = 11.4$ mm. The screw comprised of $n_{flights} = 22$ flights with diameter, $D_{flight} = 12.7$ mm and width, $L_{flight} = 2.51$ mm. At a screw speed, $\dot{N} = 30$ rpm, 60 g of the polymer took approximately 4.5 min to convey through the extruder (with die) resulting in a volumetric flow rate, $\dot{Q} = 12.7$ cm³/min. The residence time, t_{res} (at 30 rpm) was thus 1.33 min. Note that the information pertaining to the screw designs for the twin-screw extruder is proprietary.

Table 1
Sample labels and processing conditions.

Sample Name	Processing equipment	Screw Speed, $\dot{N}$ (rpm)	Accumulated Strain, γ_{acc}
GM-300	Twin Screw Extruder utilizing Gear Mixers (TSE - GM)	300	2000
GM-400	Twin Screw Extruder utilizing Gear Mixers (TSE - GM)	400	2500
KB-300	Twin Screw Extruder utilizing Kneading Blocks (TSE - KB)	300	2700
KB-400	Twin Screw Extruder utilizing Kneading Blocks (TSE - KB)	400	3510
SSE	Single Screw Extruder	30	2020
Mixer	Brabender Mixer with Banbury blades	60	1575

2.2. Ultra small-angle X-ray scattering (USAXS)

Five to ten pellets from each sample were hot pressed at about 120 °C for 3 min to create 1 mm thick discs for USAXS measurements. Ultra-small angle X-ray scattering studies on these pressed sample discs were conducted at beamline 9-ID C at the Advanced Photon Source, Argonne National Laboratory, IL, USA. The instrument is designed and operated by Jan Ilavsky and his team [43,44]. All scattering data was analyzed on IGOR Pro®. The absolute intensity data was reduced and de-smeared prior to analysis using the Irena suite [45] in IGOR Pro®. Note that the polymer background was subtracted prior to performing the Unified Fits [19,26,27], equation (1), on the dilute, ϕ_0 (1 wt%) samples and fits based on the mean-field model, equations (2) and (3), for the higher concentration (ϕ) samples using the dilute parameters for $I_0(q)/\phi_0$.

2.3. Scanning electron microscopy (SEM)

Another set of discs were hot pressed at 120 °C for about 1 min by utilizing a single pellet from each extruder and mixer to achieve a sample thickness about 100 μm thick. These samples were sputter coated with gold prior to imaging via a scanning electron microscope. Micrographs were obtained on a SCIOS Dual-Beam Scanning Electron Microscope/Focused Ion Beam at the Advanced Material Characterization Center (AMCC) at University of Cincinnati. The micrographs were obtained for samples containing the highest volume fraction (ϕ) of carbon black at an operating voltage of 5 kV and an operating current of 0.1 nA at 50,000 times magnification.

3. Results

3.1. Characterization of the carbon black-polystyrene nanocomposites processed on each mixing geometry through scattering and microscopy

Fig. 5 shows SEM micrographs for the highest carbon black loaded ($\phi_{wt} = 0.20$) samples processed on the twin-screw extruder (a) GM-300, (b) GM-400, (c) KB-300, (d) KB-400; single screw extruder (e) SSE; and (f) mixer. In each micrograph the dark grey area represents the polystyrene matrix whereas the lighter areas indicate carbon black aggregates. Some asperities indicated by craters on the otherwise smooth surface are also seen in Fig. 5(a), potentially due to inadequate sample preparation. As such, any meaningful information such as the average area occupied by the filler aggregates, the average aggregate size and the mean separation distance between the aggregates cannot be ascertained from the micrographs as is. To characterize the filler particles from the SEM images, a 500 by 500-pixel section of each SEM image was selected and inverted in color using Adobe Photoshop Elements 2019 as shown in the binary images adjacent to the SEM micrographs in Fig. 5. The width of the image, 1623.4 nm, was then calculated by measuring the number of pixels in the scale bar. The resulting binary images compared well to the original grayscale images at a thresholding value of 135. Varying this value resulted in making the filler and polymer matrix indistinguishable. Note that the binary image for GM-300 in Fig. 5(a) required manual corrections to remove the surface asperities, however a rigorous treatment was not performed to eliminate bias. In the binary images in Fig. 5, it is observed that the average end-to-end distance of the carbon black aggregates is similar across all mixing geometries at the corresponding strains. The larger blotches represent aggregates on the imaging plane whereas the small, dot-like features represent aggregates out of the imaging plane. Although the average aggregate size can be quantified, other topographical features cannot be resolved.

Fig. 6 shows the reduced (concentration normalized) scattering intensity, $I_0(q)/\phi_0$, as a function of the reciprocal space vector, q, for the dilute filler samples ($\phi_0 = 0.005$), (a) GM-300, (b) GM-400, (c) KB-300, (d) KB-400, (e) SSE, and (f) mixer. The corresponding Unified fits, equation (1) solid black curve, are also shown. In Fig. 6(e) and (f), the
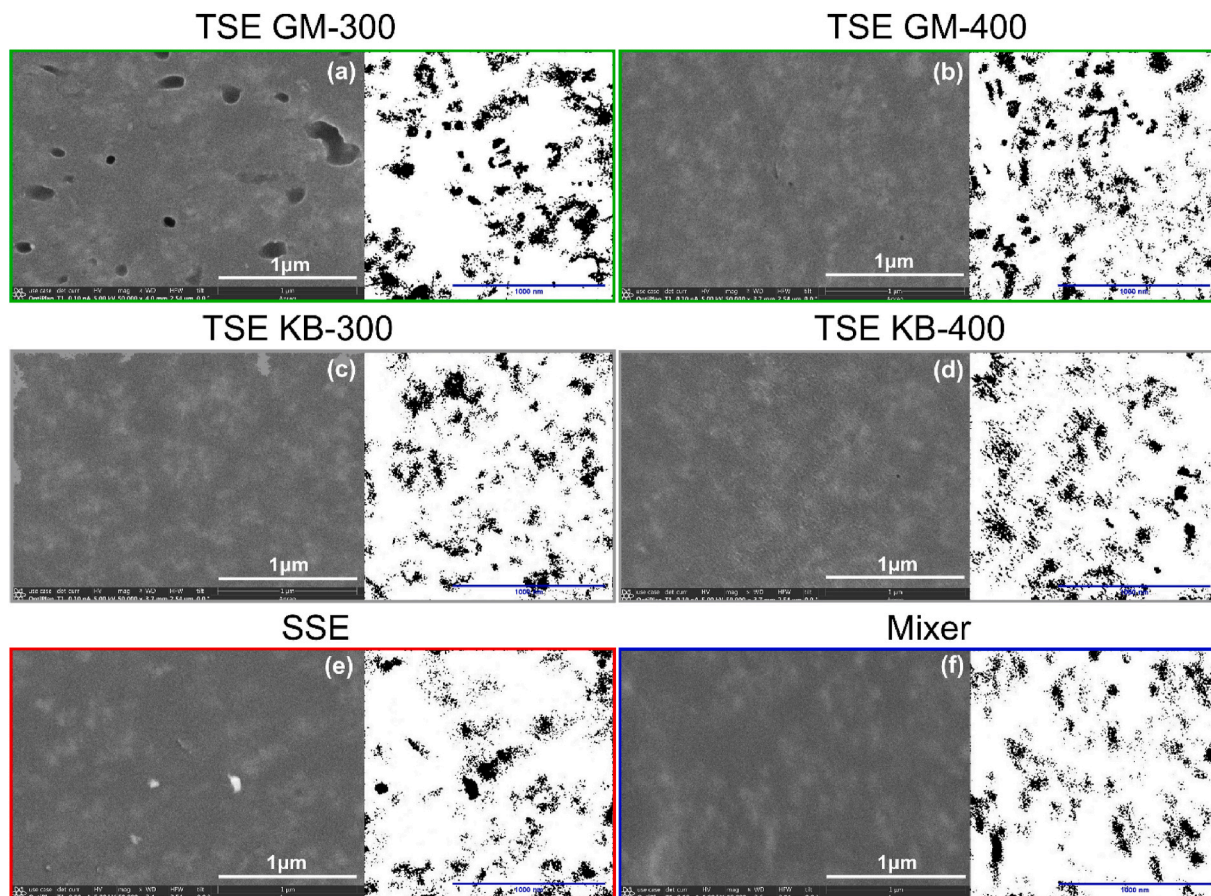
Fig. 5. Scanning electron micrographs of highest ($\phi_{wt} = 0.20$) carbon black filler loaded polystyrene samples prepared on a twin-screw extruder (a) GM-300, (b) GM-400, (c) KB-300, (d) KB-400, single-screw extruder (e) SSE, and a Banbury (f) mixer. The dark grey areas represent the polymer matrix whereas the lighter regions represent the filler aggregates. The binary images adjacent to the greyscale images depict a 500 by 500-pixel section processed from the SEM micrographs to distinguish the filler and polymer matrix. In these images, the black areas represent the filler aggregates whereas the white regions represent the polymer matrix. Color boxes around the images correlate with the colored curves in Fig. 6. (For interpretation of the references to color in this figure legend, the reader is referred to the Web version of this article.)

region to the left of the dashed line i.e., $q < 0.0007$ Å^{-1} in (a)-(d) and $q < 0.0008$ Å^{-1}, characterize the largest hierarchical structures that can be observed on the combined USAXS/SAXS scale which are compact agglomerated carbon black aggregates as reflected by the low-q power law slope ($-3 \leq P_3 \leq -4$). Note that the corresponding low-q Guinier knee is not observed for these compact agglomerates due to the experimental limits. For quantification of dispersion of nanoaggregates made up of primary particles, we limit the Unified fit, equation (1), to the first two structural levels as shown by the black curve, between the two dotted black lines. Note that the Unified fit shown in Fig. 6(a)–(f) only shows the components associated with the aggregates the low-q scattering region. The first structural level is characterized by the observed power law slope of -4 and the corresponding Guinier knee in the high-q region (0.007 Å^{-1}< q < 0.02 Å^{-1}). On the contrary, the second structural level is characterized by a power law slope, $-2 \leq P_2 \leq -3$ and the corresponding Guinier knee in the mid-q region ($\sim$0.0007 Å^{-1} < q < 0.007 Å^{-1}). This indicates that the nanoaggregates are mass-fractal entities made up of z primary particles obtained from the fit parameters to the Unified function tabulated in Table A1 in the Supplementary Information. At much larger q, the structure of graphitic sheets that make up the primary particles can be resolved, although this is beyond the scope of the discussion in this article.

The left inset images in Fig. 6 show the average aggregate based on the Unified fit results. These aggregates were simulated in IGOR Pro® [45] based on a simulation method proposed by Mulderig et al. [28] that uses the values from the USAXS parameterization to generate 3D

structures. Notice that these aggregates qualitatively compare well with the SEM images of a single aggregate taken from the corresponding binary images in Fig. 5. The SEM and 3D USAXS models match well in size though the micrographs are slightly less magnified in Fig. 6.

3.2. Impact of varying mixing/extrusion conditions on the carbon black nanoaggregates in polystyrene – dispersive (breaking apart) mixing

The primary particle and aggregate size as well as the topological dimensions, listed in Table A2 in the Supplementary Information were derived from the Unified fit parameters listed in Table A1 in the Supplementary Information, as discussed previously. These experimental topological parameters agree within error with those of the simulated 3D aggregates in Table A2 in the Supplementary Information. Fig. 7 shows the trends for (a) average primary particle size, d_p, (b) the degree of aggregation, z, (d) the mass-fractal dimension, d_f, the minimum dimension of the short-circuit path, d_{min} and the aggregate connectivity dimension, c as a function of the accumulated strain, γ_{acc}, experienced by the aggregates during the mixing process as listed in Table 1. d_p decreases with accumulated strain in Fig. 7(a). Within one mixing geometry (green or grey points) there is no change in d_p, while across mixing geometries a reduction is seen indicating that for higher strain with a smaller gap for different mixing geometries the associated increase in laminar mixing serves to break up the primary particle clusters depicted in Fig. 3. The reduction in primary particle size results in an increase in the degree of aggregation, z, as shown in Fig. 7(b). This is expected since
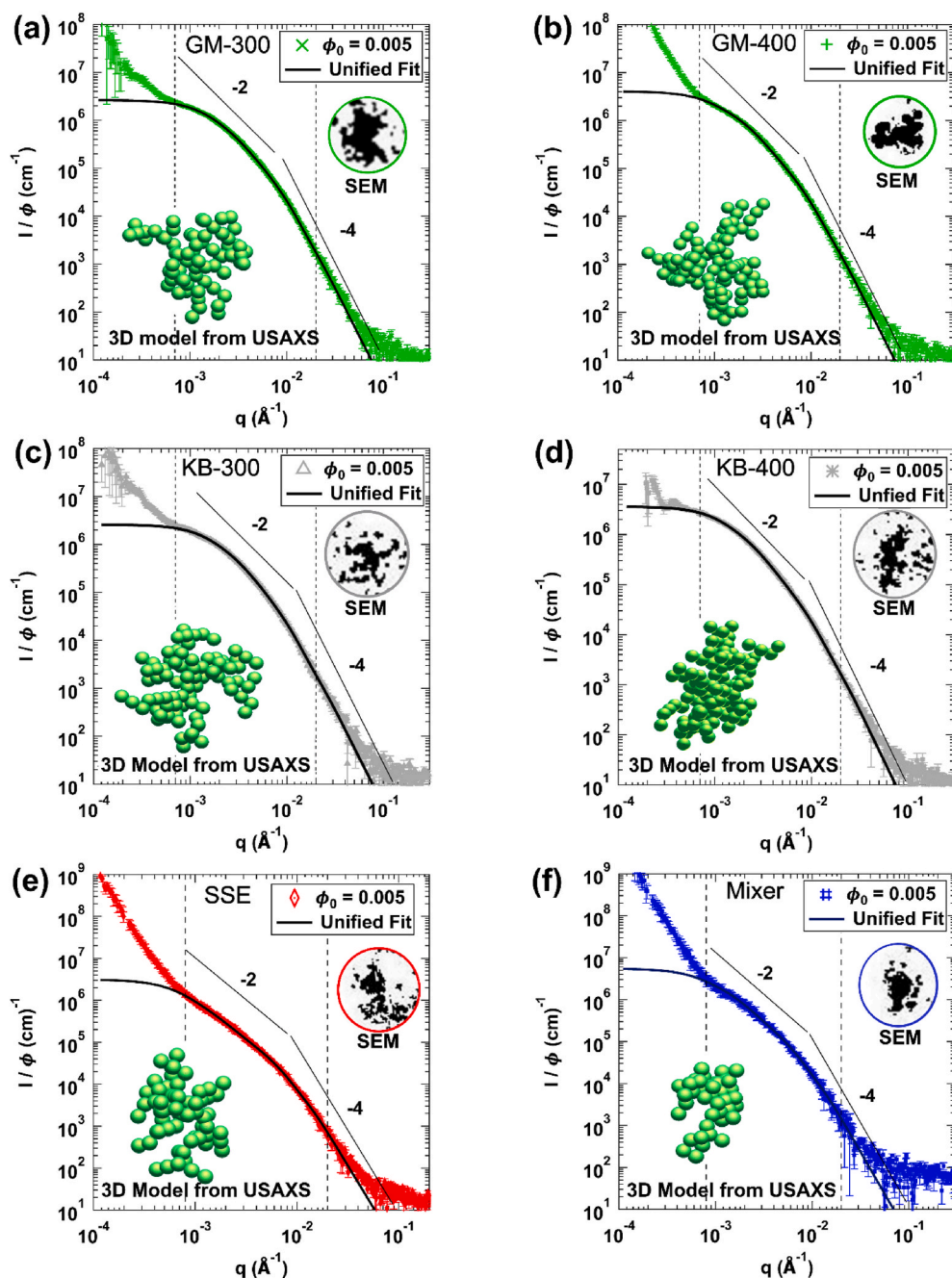
Fig. 6. Reduced USAXS curves, $I_0(q)/\phi_0$ at dilute carbon black volume fraction, $\phi_0 = 0.005$ for screw designs (a) GM-300, (b) GM-400, (c) KB-300, (d) KB-400, (e) SSE, and (f) mixer as a function of the reciprocal space vector, q. Note that q is inversely related to structural size so large q represents smaller features and vice versa. Each plot shows the Unified fit (equation (1), black curve) for q ranging between the dashed lines. The fit within this q-range accounts for the level 1 primary particles and the level 2 aggregate of the structural hierarchy. The left inset image in each figure shows the simulated aggregate with topological parameters comparable to the scattering results as detailed in Table A2 in the Supplementary Information. This aggregate simulation code is based on the model proposed by Mulderig et al. [28] and optimized in IGOR Pro® by Ilavsky et al. [45] The right inset image shows an SEM aggregate from Fig. 5 for qualitative comparison with the 3D aggregate model.

smaller nanoparticles, have a larger surface to volume ratio (S/V), $1/d_p$, so the increase in z could be driven by a reduction in surface area as shown in Fig. 7(c). This dependence on S/V seems universal for different fillers subject to different processing conditions and has been demonstrated for carbon-coated silica fillers in styrene-butadiene rubber processed on a Banbury mixer [46]. The trend in Fig. 7(c) predicts a $d_{p,max}$ of about 64 nm, above which in d_p, aggregation is not expected. This result is not unexpected since the N330 grade of carbon black (low-structure as compared to the N110 grade) characterized by a specific surface area of 80 m^2/g and Sauter mean diameter ($d_p = 6\ V/S$) of 41.5 nm [42] forms aggregates of about 10 primary particles post mixing in the Banbury mixer [7]. The constant d_p for the same mixing geometry (grey and green points) seen in Fig. 7(a) is not seen in z where a more linear dependence in accumulated strain for z is observed across mixing geometries in Fig. 7(b). This might be an impact of increased collision frequency between primary particles and aggregates with higher

distributive mixing.

Fig. 7(d) shows that the mass-fractal dimension of the aggregates, d_f, increases with increasing γ_{acc}, indicating denser aggregates. This increase in aggregate density offsets the increase in z and results in essentially a constant aggregate size, R_{eted}, with increasing γ_{acc} as shown by the orange circles in Fig. 7(f), although a reduction in aggregate size is expected at larger strains [47–49]. The average feature size estimated using ImageJ from the SEM micrographs after image processing in Fig. 5 shows a similar trend to the USAXS estimates depicted by the blue triangles in Fig. 7(f). Fig. 7(d) compares the variation in the aggregate topological parameters, d_{min} and c with accumulated strain. When $c = 1$, i.e., $d_f = d_{min}$, the aggregates are linear unbranched chains. On the contrary, for $c \sim d_f$, the aggregates are completely branched and $d_{min} = 1$. Increasing c with accumulated strain results from increased branching of the aggregates that leads to denser aggregates as reflected by an increase in d_f. Fig. 7(e) shows the calculated branch fraction, ϕ_{br}, which
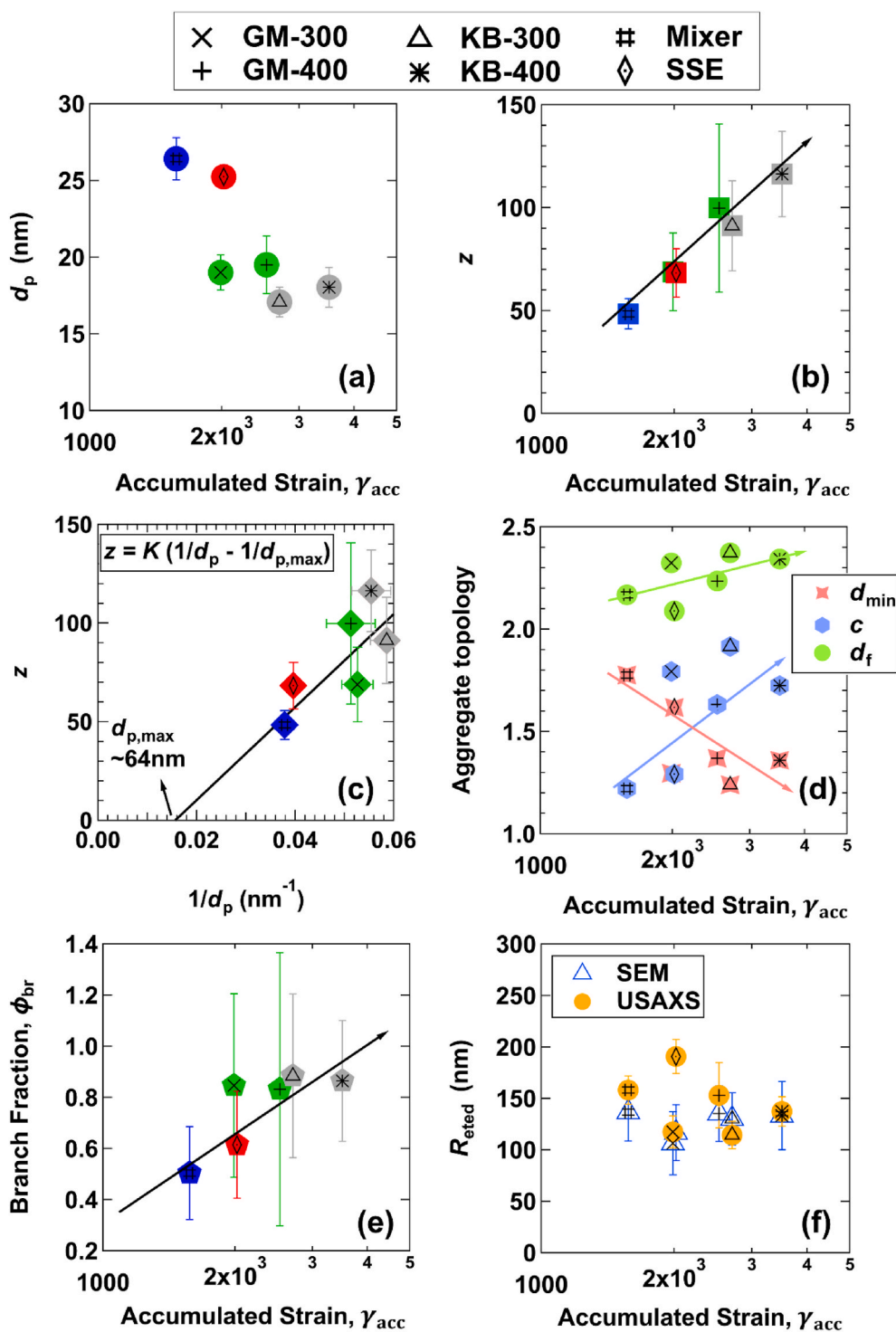
Fig. 7. Plots illustrating the (a) primary particle size, $d_p \sim V/S$, (b) degree of aggregation, z, as a function of the accumulated strain, γ_{acc}, listed in Table 1. (c) Shows the dependence of z on $S/V \sim 1/d_p$. (d) Shows an increase in connectivity dimension, c, with strain reflecting an increase in branching, with a decrease in minimum dimension, d_{min}, leading to an overall densification of the carbon aggregates with strain, d_f increases. (e) Shows the increased branching of the carbon black aggregates, ϕ_{br}, with accumulated strain while the overall aggregate size, R_{eted}, remains constant (f) and the values from SEM and USAXS agree.

varies from 0 to 1. Processing the filled-composites in the SSE and mixer result in more chain-like aggregates with a smaller branch content (refer Table A2 in the Supplementary Information), whereas processing on the TSE results in highly branched aggregates. These differences are also observed in the simulated aggregates shown in the inset images in Fig. 6 (a)–(f). Like the trend between mixing geometries in Fig. 7(a) where the green and grey points show constant d_p, the branch fraction in one geometry (green and grey points) remains almost constant with increased accumulated strain in Fig. 7(e). A similar behavior is seen with "c" in Fig. 7(d). This indicates that the mix of laminar and turbulent flow, which changes across mixing geometries, may play an important role for

these parameters.

3.2.1. Large-scale structural dispersion

At lowest-q, Figs. 6 and 8(a), the power-law reflects the organization of large, micron-scale structures. This low-q slope ($q < 0.0005\,\text{Å}^{-1}$ or the vertical dashed black line in Fig. 8) for all semi-dilute filler concentrations ($\phi > 0.005$) in Fig. 8(a) for KB-300 is like the dilute sample ($\phi_0 = 0.005$) and ranges between -3 and -4 indicating rough surfaced solid agglomerates of aggregates and the absence of a global-filler network in this concentration range and for these processing conditions. Notice that this phenomenon is also observed at all semi-dilute filler concentrations
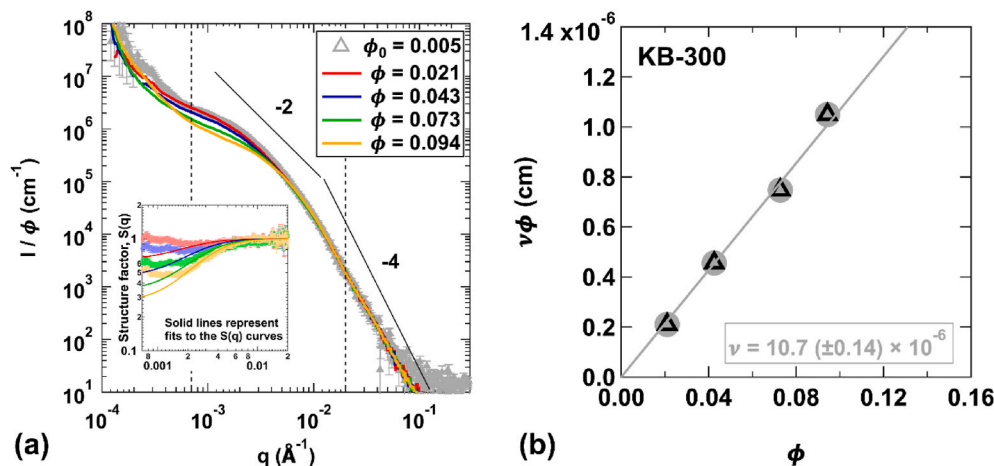
Fig. 8. (a) USAXS curves for carbon black/polystyrene nanocomposite processed in the twin-screw extruder operated at 300 rpm with screw design utilizing KB. The dilute scattering curve, $I_0(q)/\phi_0$, was fit using equation (1) for 0.0007 Å^{-1} $< q <$ 0.02 Å^{-1}, i.e., the region within the dashed lines. Increasing filler concentration results in a reduction in the $I(q)/\phi$ curves in the region associated with the aggregate structural level between the dashed lines indicating aggregate overlap. The corresponding structure factor, $S(q)$, obtained by normalizing $I(q)/\phi$ by $I_0(q)/\phi_0$ within this region is shown in the inset figure. These $S(q)$ curves were fit using equation (3) to quantify the extent of screening/overlap, $\phi\nu$. (b) A plot of $\phi\nu$ as a function of the filler concentration ϕ determines the effective interaction parameter, ν. For all other nanocomposites, refer to Figs. S1–S5 in the Supplementary Information.

for the SSE and Mixer samples in Fig. S4(a) and Fig. S5(a), respectively, in the Supplementary information. However, the KB-400 samples display a micron-scale, mass-fractal agglomerate network of nano-aggregates (low-q slopes ranging between −1 and −3) at the highest concentration of $\phi = 0.120$ (orange curve in Fig. S3(a) in the Supplementary Information), while there are not enough data points at low-q for $\phi = 0.080$ (green curve in Fig. S3(a) in the Supplementary Information). This large-scale network is important for bulk conductivity, and mechanical strength and is generally a target structure for this type of nanocomposite. Contrary to this, semi-dilute samples processed using gear mixers on the twin-screw extruder at both 300 rpm and 400 rpm show the presence of a global mass-fractal network on the micron scale as shown in Fig. S1(a) and Fig. S2(a) in the Supplementary Information, except for $\phi = 0.085$ (green curve in Fig. S1(a) in the Supplementary Information). In the concentration range studied here, it seems that low-shear conditions lead to the absence of a filler network on the micron scale which is detrimental to the bulk mechanical properties and conductivity. From these scattering observations it is expected that the SEM micrographs in Fig. 5(a) and (b), Fig. 5(d) should show a network structure while Fig. 5(c) and (e), Fig. 5(f) should show 3D agglomerates. This seems to be possible from the original micrographs, but the network feature is lost in the thresholding figures.

The calculated accumulated strain for the mixers in increasing order are Mixer < GM-300 ∼ SSE < GM-400 < KB-300 < KB-400. There is no clear relationship between the calculated accumulated strain and the appearance of a macroscopic network. However, as shown below, there seems to be a link between the nano-distributive mixing as measured by B_2^* and the presence of a macroscopic filler network with the lowest distributive mixing samples inclined to form macroscopic networks consistent with a previously proposed model that nano-scale immiscibility is necessary for the formation of macroscopic networks. For B_2^* the order of mixers are Mixer > SSE > GM-400 > KB-400 > KB-300 > GM-300, with only KB-300 not displaying a macroscopic network for the low B_2^* samples.

3.3. Distributive (organizational) mixing of carbon black nanoaggregates in polystyrene for different mixing/extrusion conditions

3.3.1. Estimation of the effective interaction parameter, ν, from scattering

Fig. 8(a) compares the reduced scattering curves, $I(q)/\phi$, at semi-dilute concentrations, $\phi = 0.021$ (red), 0.043 (blue), 0.073 (green), and 0.094 (orange) with the dilute curve, $I_0(q)/\phi_0$, where $\phi_0 = 0.005$ for KB-300 samples. Similar curves for GM-300, GM-400, KB-400, SSE and Banbury mixer are shown in Fig. S1(a), Fig. S2(a), Fig. S3(a), Fig. S4(a),

and Fig. S5(a), respectively, in the Supplementary Information.

The experimental volume fraction does not correctly account for the filler volume fraction in the 0.8 mm USAXS beam footprint due to fluctuations in concentration across the sample. For this reason, is it more accurate to determine the volume fraction, ϕ, by scaling $I(q)$ at the highest q to the dilute sample, $I_0(q)/\phi_0$, such that the two curves overlap in the high-q region.

The structure factor, $S(q)$, shown in Fig. 8(a) inset and Figs. S1(a)–S5 (a) insets in the Supplementary Information is determined from the ratio of $I(q)/\phi$ and $I_0(q)/\phi_0$. Since the Unified fit is limited to the first two structural levels in the region between the two dashed lines in Fig. 8(a) and Figs. S1(a)–S5(a) in the Supplementary Information, the inset $S(q)$ curves are only shown within this region of scattering vector. Notice that $S(q) = 1$ for 0.008 Å^{-1} $< q <$ 0.02 Å^{-1} since the dilute and semi-dilute curves overlap in this range, whereas, for 0.002 Å^{-1} $< q <$ 0.008 Å^{-1}, $S(q)$ is reduced. Equation (3) fit the data well within these two q ranges, however, for 0.0007 Å^{-1} $< q <$ 0.002 Å^{-1} the fit does not agree with the data. This apparent deviation at low-q can be attributed to agglomerates of nano-aggregates that makeup the third structural level (either 3D agglomerates or a mass-fractal filler network) as mentioned previously. These agglomerates are not accounted for in equation (3). Nonetheless, from the fits, the value of $\nu\phi$ can be determined for each filler concentration, ϕ, in the limit of $q \to 0$. Fig. 8(b) shows plots of the aggregate structural screening, $\nu\phi$, as a function of the filler volume fraction, ϕ for the KB-300 nanocomposite processed on the TSE. Similar plots for GM-300, GM-400, KB-400, SSE, and mixer are shown in Fig. S1(b), Fig. S2 (b), Fig. S3(b), Fig. S4(b), and Fig. S5(b), respectively, in the Supplementary Information. A linear dependence with ϕ for all samples indicates that the filler-filler interaction is dominated by binary interactions in this concentration range (only the second virial term is needed in the virial expansion). The proportionality constant or the effective interaction parameter, ν, corresponds to the slope of the straight-line fits to the data.

3.3.2. Quantification of filler distribution (organization) via scattering and microscopic analysis

To quantify the macroscopic filler distribution (organization) through SEM micrographs, the average free space, $L_{f,avg}$, was used. The free space between filler aggregates from each micrograph, $L_{f,j}$, was determined using the MATLAB code of Khare and Burris [50] for the processed binary images shown in Fig. 5. This code measures the occurrence of filler aggregates in ∼10,000 random squares with varying sizes in binary images processed from the micrographs. The code returns the largest square of free space of size $L_{f,j}$ with less than 0.005

probability to have no particles. To determine the standard deviation and $L_{f,avg}$, four images were created by dividing each sample's binary image into four corner sections as shown in the center image in Figs. S7–S12 in the Supplementary Information. Each corner section was then copied to create new 500 by 500-pixel images as shown in Figs. S7–S12 in the Supplementary Information. $L_{f,j}$ from these four binary images and the original binary image in Fig. 5 were used to calculate the standard deviation and $L_{f,avg}$. Note that the area fraction, ϕ_A, from the processed SEM micrographs and the volume fraction, ϕ_V (or ϕ), from scattering are comparable as shown in Fig. S6 in the Supplementary Information.

Fig. 9 shows a plot of the extent of nano distributive mixing quantified using B_2^* through scattering (red circles, left axis) as a function of the inverse accumulated strain, $1/\gamma_{acc}$ (refer Table 1), for each mixing geometry and mixing condition. This plot follows van der Waals model [6,7], $B_2^* = b^* - (a^*/\gamma_{acc})$, equation where b^* is the excluded volume including bound polymer and a^* is the attractive potential between carbon aggregates. A negative slope and a positive intercept are necessary by this analysis since the carbon black cannot be repulsive and must have a positive excluded volume. It was previously shown for the Banbury mixer and for the single screw extruder that carbon black and silica nanocomposites in elastomers and in polystyrene could be well described by the van der Waals model [5–7,34,46,51]. For the KB and GM TSEs in Fig. 9 the decreasing B_2^* values and positive intercept within a given extruder geometry also follows the van der Waals function, as indicated by the two downward sloped dashed lines and arrow. Differences between the two mixing geometries involve different intercepts to the negative slopes which indicate different b^* values. b^* changes when the amount of bound polymer changes so the two mixing geometries may result in different amounts of bound polymer. However, across different mixing geometries a positive slope is observed, top arrow, which is not consistent with the van der Waals model using γ_{acc} and an analogy to $k_B T$. This upward trend, as indicated by the upward arrow, is also followed by the macroscopic SEM measures of distributive

Fig. 9. The extent of dispersion quantified using B_2^* from scattering (red circles) and the average free space, $L_{f,avg}$, from micrograph analysis (blue triangles) as a function of the inverse accumulated strain, $1/\gamma_{acc}$. $L_{f,avg}$ is for the highest filler loading, while B_2^* is calculated from a concentration series. Within a given mixing geometry the van der Waals model is followed, inset equation and downward arrows. Between mixing geometries an upward slope is seen which may reflect increased laminar flow for higher accumulated strain at smaller flow gaps. Laminar flow enhances dispersive (breakup) mixing over distributive mixing. (For interpretation of the references to color in this figure legend, the reader is referred to the Web version of this article.)

mixing (blue triangles).

One explanation for the anomalous behavior across mixing geometries is that the fraction or degree of laminar versus turbulent flow changes with different mixing geometries. As mentioned earlier, for thinner gaps, which lead to larger accumulated strain, dispersive mixing becomes much more difficult since thin gaps generally display low Reynolds numbers and laminar flow versus wider flow gaps that display lower accumulated strain but larger Reynolds numbers, equations (13) and (14) below. For flow in a gap with the top surface moving and the bottom surface fixed the Reynolds number is defined as,

$$Re = \rho v G / \eta \tag{13}$$

where, ρ is the melt density, v is the velocity of the top plate, G is the flow gap distance, and η is the melt viscosity. Generally, $Re < 200$ is laminar and $Re > 10,000$ is turbulent, but 2000 is often used as a cutoff value with some contribution from laminar and turbulent flow between 200 and 10,000. For the same conditions the accumulated strain is given by,

$$\gamma_{acc} = t\,\mathrm{d}v/\mathrm{d}y = tv/G \tag{14}$$

where, t is the mixing time. An appropriate measure of the extent and amount of turbulent flow that leads to distributive mixing might be,

$$Re_{acc} = tRe = \rho\gamma_{acc} G^2 / \eta \tag{15}$$

Due to the complexity of the geometry in mixers, and the dependence of viscosity on shear rate and filler concentration it is not feasible to calculate Re_{acc} in this study, but we plan to investigate a simple geometry where the melt flow gap can be varied in a controlled manner to test the appropriateness of equation (15). The van der Waals dependence would then become,

$$B_2^* = b^* - (a^* / Re_{acc}) \tag{16}$$

Within a single mixing geometry and for a fixed polymer and temperature, equation (15) indicates that Re_{acc} is proportional to γ_{acc} supporting the observed van der Waals behavior in Fig. 9. From the almost linear dependence of B_2^* as a function of $1/\gamma_{acc}$ seen across mixing geometries in Fig. 9, it seems that there is close to a proportionality between the inverse of the accumulated strain and $1/Re_{acc}$ and the extent of turbulent flow in the mixing geometries which serves to increase B_2^*.

Since the macroscopic measure of mixing, $L_{f,avg}$, does not display van der Waals behavior (a decrease in B_2^* as a function of $1/\gamma_{acc}$) even within the same mixing geometry, that is for GM-300 and GM-400 or for KB-300 and KB-400, it would seem that the macroscopic measure may be more sensitive to distributive (breakup) mixing while the nanoscale measure, B_2^*, is sensitive to both distributive as well as dispersive mixing.

4. Conclusions

Dispersion and distribution of nanoparticles in nanocomposites are major obstacles to the enhancement of properties in nanomaterials. Mixing depends on simple factors such as mixing speed, mixing time and more complex factors such as mixing geometry. In this paper the impact on dispersive and distributive mixing of mixing geometry was explored. It was found that dispersion and breakup of carbon black in polystyrene followed simple trends in the accumulated strain regardless of the mixing geometry with increased accumulated strain leading to a reduction in primary particle size and an associated increase in aggregation that was proportional to the S/V ratio of the filler primary particles. While the degree of aggregation increased, the aggregate size remained almost constant because the topology of the carbon black aggregates increased density through branching. The dispersive mixing also involved formation of two types of large-scale structures, 3D agglomerates of aggregates or mass-fractal networks of aggregates that percolate to fill space providing reinforcement and electrical

conductivity. Formation of these large-scale emergent structures were not linear in accumulated strain but depended on the details of the mixing geometry and mixing speed. A correlation with poor nanoscale distributive mixing, B_2^*, was shown supporting the concept that local immiscibility is necessary for the formation of macroscopic filler networks and their associated improvement in properties such as tear strength and conductivity.

Distribution of nanoparticles was seen to follow the van der Waals model when considering a given mixing geometry and variable mixing speed, agreeing with previous studies. However, when comparing different mixing geometries that display different flow gaps and concomitant variation in laminar and turbulent flow it is seen that increases in accumulated strain, associated with thinner flow gaps and reduced Reynolds number results in worse distributive mixing, the opposite of the prediction of the van der Waals model. It was proposed that the accumulated Reynolds number may be a better parameter to correlate different mixing geometries and mixer speeds, Re_{acc}.

Macroscopic measures of mixing using SEM micrographs and statistical analysis did not display van der Waals behavior even for variable mixing speed within a given geometry but did indicate that dispersive (breakup) mixing was enhanced with thinner mixing gaps. This shows some advantages for nanoscale measures of mixing for these systems using USAXS.

This study reveals some of the complexities that might be expected in ab initio prediction of mixing for nanocomposites and some of the nuances that might be encountered in understanding mixing using macroscopic and nanoscale techniques. Generally, dispersive (breakup) mixing is well characterized by the accumulated strain across different mixing geometries, while distributive mixing depends greatly on the mixing geometry and the extent of turbulent vs laminar flow. Within one mixing geometry the accumulated strain can be used to model distributive mixing in addition to dispersive mixing.

Notes

The authors declare no competing financial interest.

Disclaimers

The findings and conclusions in this report are those of the author(s) and do not necessarily represent the official position of the National Institute for Occupational Safety and Health, Centers for Disease Control and Prevention.

CRediT authorship contribution statement

Danielle Veigel: Validation, Formal analysis, Investigation, Writing – original draft, Writing – review & editing, Visualization. **Kabir Rishi:** Conceptualization, Methodology, Software, Investigation, Resources, Data curation, Writing – original draft, Writing – review & editing, Visualization, Supervision, Project administration. **Ugochukwu Okoli:** Investigation, Writing – review & editing, Visualization. **Gregory Beaucage:** Conceptualization, Methodology, Software, Resources, Writing – review & editing, Visualization, Supervision, Project administration, Funding acquisition. **Jeffrey A. Galloway:** Conceptualization, Methodology, Investigation, Writing – review & editing. **Hannah Campanelli:** Investigation. **Jan Ilavsky:** Investigation. **Ivan Kuzmenko:** Investigation. **Melodie Fickenscher:** Investigation.

Declaration of competing interest

The authors declare the following financial interests/personal relationships which may be considered as potential competing interests: Gregory Beaucage reports financial support was provided by National Science Foundation. Gregory Beaucage reports financial support was provided by US Department of Energy Office of Science.

Data availability

Data will be made available on request.

Appendix A. Supplementary data

Supplementary data to this article can be found online at https://doi.org/10.1016/j.polymer.2023.125735.

References

[1] Z. Tadmor, C.G. Gogos, Principles of Polymer Processing, second ed., John Wiley & Sons, Inc., Hoboken, NJ, USA, 2006.

[2] A.A. Griffith, VI. The phenomena of rupture and flow in solids, Philos. Trans. R. Soc. Lond. - Ser. A Contain. Pap. a Math. or Phys. Character 221 (1921) 163–198, https://doi.org/10.1098/rsta.1921.0006.

[3] E. Orowan, Fracture and strength of solids, Rep. Prog. Phys. 12 (1949) 309, https://doi.org/10.1088/0034-4885/12/1/309.

[4] G.R. Irwin, Fracture, in: Handb. Der Phys. Band VI, Elastizität Und Plast, Springer-Verlag, Berlin, 1958.

[5] Y. Jin, G. Beaucage, K. Vogtt, H. Jiang, V. Kuppa, J. Kim, J. Ilavsky, M. Rackaitis, A. Mulderig, K. Rishi, V. Narayanan, A pseudo-thermodynamic description of dispersion for nanocomposites, Polymer (Guildf). 129 (2017) 32–43, https://doi.org/10.1016/j.polymer.2017.09.040.

[6] A. McGlasson, K. Rishi, G. Beaucage, V. Narayanan, M. Chauby, A. Mulderig, V. K. Kuppa, J. Ilavsky, M. Rackaitis, The effects of staged mixing on the dispersion of reinforcing fillers in elastomer compounds, Polymer (Guildf) 181 (2019), 121765, https://doi.org/10.1016/j.polymer.2019.121765.

[7] K. Rishi, V. Narayanan, G. Beaucage, A. McGlasson, V. Kuppa, J. Ilavsky, M. Rackaitis, A thermal model to describe kinetic dispersion in rubber nanocomposites: the effect of mixing time on dispersion, Polymer (Guildf) 175 (2019) 272–282, https://doi.org/10.1016/j.polymer.2019.03.044.

[8] J.G. Drobny, Handbook of Thermoplastic Elastomers, second ed., Elsevier Inc., 2014.

[9] W. Schuler, Process Engineering Design of Co-rotating Twin Screw Extruders, University of Wales, Swansea, 1996.

[10] C. Rauwendaal, Polymer Extrusion, fifth ed., Carl Hanser Verlag GmbH Co KG, Munich, Germany, 2014.

[11] B. Dryer, G. Fukuda, J. Webb, K. Montemayor, D.I. Bigio, P. Andersen, M. Wetzel, Comparison of scale-up methods for dispersive mixing in twin-screw extruders, Polym. Eng. Sci. 57 (2017) 345–354, https://doi.org/10.1002/pen.24439.

[12] D. Bigio, W. Pappas, H. Brown II, B. Debebe, W. Dunham, Residence shear distribution in a twin screw extruder, in: Proc. 69th Annu. Tech. Conf. Soc. Plast. Eng., Boston, Massachusetts, 2011, pp. 1382–1386. https://www.tib.eu/en/search/id/BLCP:CN079794660/RESIDENCE-STRESS-DISTRIBUTIONS-IN-TWIN-SCREW-EXTRUDERS?cHash=a528f5ced7391393fbbe9d1b13890f4f.

[13] A. Stevenson, A. Jones, S. Raghavan, Characterization of particle dispersion and volume fraction in alumina-filled epoxy nanocomposites using photo-stimulated luminescence spectroscopy, Polym. J. 43 (2011) 923–929, https://doi.org/10.1038/pj.2011.82.

[14] I. Hanhan, A. Selimov, D. Carolan, A.C. Taylor, S. Raghavan, Quantifying alumina nanoparticle dispersion in hybrid carbon fiber composites using photoluminescent spectroscopy, Appl. Spectrosc. 71 (2017) 258–266, https://doi.org/10.1177/0003702816662623.

[15] L. Hui, R.C. Smith, X. Wang, J.K. Nelson, L.S. Schadler, Quantification of particulate mixing in nanocomposites, Annu. Rep. - Conf. Electr. Insul. Dielectr. Phenomena, CEIDP. (2008) 317–320, https://doi.org/10.1109/CEIDP.2008.4772831.

[16] L. Song, Z. Wang, X. Tang, L. Chen, P. Chen, Q. Yuan, L. Li, Visualizing the toughening mechanism of nanofiller with 3D X-ray nano-CT: stress-induced phase separation of silica nanofiller and silicone polymer double networks, Macromolecules 50 (2017) 7249–7257, https://doi.org/10.1021/acs.macromol.7b00539.

[17] T. Hashimoto, N. Amino, S. Nishitsuji, M. Takenaka, Hierarchically self-organized filler particles in polymers: cascade evolution of dissipative structures to ordered structures, Polym. J. 51 (2019) 109–130, https://doi.org/10.1038/s41428-018-0147-2.

[18] K. Rishi, G. Beaucage, V. Kuppa, A. Mulderig, V. Narayanan, A. McGlasson, M. Rackaitis, J. Ilavsky, Impact of an emergent hierarchical filler network on nanocomposite dynamics, Macromolecules 51 (2018) 7893–7904, https://doi.org/10.1021/acs.macromol.8b01510.

[19] G. Beaucage, Approximations leading to a unified exponential/power-law approach to small-angle scattering, J. Appl. Crystallogr. 28 (1995) 717–728, https://doi.org/10.1107/S0021889895005292.

[20] A. Guinier, G. Fournet, Small Angle Scattering of X-rays, John Wiley & Sons, New York, US, 1955.

[21] G. Porod, General theory, in: O. Glatter, O. Kratky (Eds.), Small Angle X-Ray Scatt, Academic Press Inc., New York, US, 1982, pp. 17–51.

[22] T. Koga, M. Takenaka, K. Aizawa, M. Nakamura, T. Hashimoto, Structure factors of dispersible units of carbon black filler in rubbers, Langmuir 21 (2005) 11409–11413, https://doi.org/10.1021/la051352s.

[23] T. Koga, T. Hashimoto, M. Takenaka, K. Aizawa, N. Amino, M. Nakamura, D. Yamaguchi, S. Koizumi, New insight into hierarchical structures of carbon black dispersed in polymer matrices: a combined small-angle scattering study, Macromolecules 41 (2008) 453–464, https://doi.org/10.1021/ma071867l.

[24] R. Ramachandran, G. Beaucage, A.S. Kulkarni, D. McFaddin, J. Merrick-Mack, V. Galiatsatos, Persistence length of short-chain branched polyethylene, Macromolecules 41 (2008) 9802–9806, https://doi.org/10.1021/ma801775n.

[25] D.K. Rai, G. Beaucage, E.O. Jonah, D.T. Britton, S. Sukumaran, S. Chopra, G. G. Gonfa, M. Härting, Quantitative investigations of aggregate systems, J. Chem. Phys. 137 (2012) 574–588, https://doi.org/10.1063/1.4737947.

[26] G. Beaucage, H.K. Kammler, S.E. Pratsinis, Particle size distributions from small-angle scattering using global scattering functions, J. Appl. Crystallogr. 37 (2004) 523–535, https://doi.org/10.1107/S0021889804008969.

[27] G. Beaucage, Determination of branch fraction and minimum dimension of mass-fractal aggregates, Phys. Rev. E. 70 (2004) 031401, https://doi.org/10.1103/PhysRevE.70.031401.

[28] A. Mulderig, G. Beaucage, K. Vogtt, H. Jiang, V. Kuppa, Quantification of branching in fumed silica, J. Aerosol Sci. 109 (2017) 28–37, https://doi.org/10.1016/j.jaerosci.2017.04.001.

[29] D.K. Rai, G. Beaucage, K. Vogtt, J. Ilavsky, H.K. Kammler, In situ study of aggregate topology during growth of pyrolytic silica, J. Aerosol Sci. 118 (2018) 34–44, https://doi.org/10.1016/j.jaerosci.2018.01.006.

[30] H.K. Kammler, G. Beaucage, R. Mueller, S.E. Pratsinis, Structure of flame-made silica nanoparticles by ultra-small-angle x-ray scattering, Langmuir 20 (2004) 1915–1921, https://doi.org/10.1021/la030155v.

[31] P.G. de Gennes, Theory of X-ray scattering by liquid macromolecules with heavy atom labels, J. Phys. 31 (1970) 235–238, https://doi.org/10.1051/jphys:01970003102-3023500.

[32] J.S. Pedersen, C. Sommer, Temperature dependence of the virial coefficients and the chi parameter in semi-dilute solutions of PEG, in: Scatt. Methods Prop. Polym. Mater, Springer Berlin Heidelberg, Berlin, Heidelberg, 2005, pp. 70–78, https://doi.org/10.1007/b107350.

[33] K. Vogtt, G. Beaucage, M. Weaver, H. Jiang, Thermodynamic stability of worm-like micelle solutions, Soft Matter 13 (2017) 6068–6078, https://doi.org/10.1039/C7SM01132F.

[34] K. Rishi, L. Pallerla, G. Beaucage, A. Tang, Dispersion of surface-modified, aggregated, fumed silica in polymer nanocomposites, J. Appl. Phys. 127 (2020), 174702, https://doi.org/10.1063/1.5144252.

[35] M. Bousmina, A. Ait-Kadi, J.B. Faisant, Determination of shear rate and viscosity from batch mixer data, J. Rheol. (N. Y. N. Y). 43 (1999) 415–433, https://doi.org/10.1122/1.551044.

[36] S. Middleman, Fundamentals of Polymer Processing, McGraw-Hill, New York, 1977.

[37] T.A. Osswald, E. Baur, S. Brinkmann, K. Oberbach, E. Schmachtenberg, International Plastics Handbook, 2006, https://doi.org/10.3139/9783446407923.fm.

[38] I. Hassinger, X. Li, H. Zhao, H. Xu, Y. Huang, A. Prasad, L. Schadler, W. Chen, L. Catherine Brinson, Toward the development of a quantitative tool for predicting dispersion of nanocomposites under non-equilibrium processing conditions, J. Mater. Sci. 51 (2016) 4238–4249, https://doi.org/10.1007/s10853-015-9698-1.

[39] Z. Kemblowski, J. Sek, Residence time distribution in a real single screw extruder, Polym. Eng. Sci. 21 (1981) 1194–1202, https://doi.org/10.1002/pen.760211804.

[40] C. Tzoganakis, Y. Tang, J. Vlachopoulos, A.E. Hamielec, Measurements of residence time distribution for the peroxide degradation of polypropylene in a single-screw plasticating extruder, J. Appl. Polym. Sci. 37 (1989) 681–693, https://doi.org/10.1002/app.1989.070370308.

[41] Technical Datasheet StyronTM 666D, Am. Styrenics LLC. (n.d.). https://amsty.com/images/documents/gpps/styron666d-tech-en.pdf (accessed December 30, 2022).

[42] W.M. Hess, G.C. McDonald, Improved particle size measurements on pigments for rubber, Rubber Chem. Technol. 56 (1983) 892–917, https://doi.org/10.5254/1.3538171.

[43] J. Ilavsky, F. Zhang, A.J. Allen, L.E. Levine, P.R. Jemian, G.G. Long, Ultra-small-angle X-ray scattering instrument at the advanced photon source: history, recent development, and current status, Metall. Mater. Trans. 44 (2013) 68–76, https://doi.org/10.1007/s11661-012-1431-y.

[44] J. Ilavsky, F. Zhang, R.N. Andrews, I. Kuzmenko, P.R. Jemian, L.E. Levine, A. J. Allen, Development of combined microstructure and structure characterization facility for in situ and operando studies at the advanced photon source, J. Appl. Crystallogr. 51 (2018) 867–882, https://doi.org/10.1107/S160057671800643X.

[45] J. Ilavsky, P.R. Jemian, Irena : tool suite for modeling and analysis of small-angle scattering, J. Appl. Crystallogr. 42 (2009) 347–353, https://doi.org/10.1107/S0021889809002222.

[46] U. Okoli, K. Rishi, G. Beaucage, H.K. Kammler, A. McGlasson, M. Chauby, V. Narayanan, J. Grammens, V.K. Kuppa, Dispersion of modified fumed silica in elastomeric nanocomposites, Polymer (Guildf) (2022), 125407, https://doi.org/10.1016/j.polymer.2022.125407.

[47] A.M. Gessler, Effect of mechanical shear on the structure of carbon black in reinforced elastomers, Rubber Chem. Technol. 43 (1970) 943–959, https://doi.org/10.5254/1.3547323.

[48] M. Klüppel, The role of disorder in filler reinforcement of elastomers on various length scales, in: Fill. Elastomers Scanning Force Microsc. Adv. Polym. Sci, Springer, Berlin, Heidelberg, 2003, pp. 1–86, https://doi.org/10.1007/b11054.

[49] C.G. Robertson, N.J. Hardman, Nature of carbon black reinforcement of rubber: perspective on the original polymer nanocomposite, Polymers 13 (2021) 1–28, https://doi.org/10.3390/polym13040538.

[50] H.S. Khare, D.L. Burris, A quantitative method for measuring nanocomposite dispersion, Polymer (Guildf). 51 (2010) 719–729, https://doi.org/10.1016/j.polymer.2009.12.031.

[51] A. McGlasson, K. Rishi, G. Beaucage, M. Chauby, V. Kuppa, J. Ilavsky, M. Rackaitis, Quantification of dispersion for weakly and strongly correlated nanofillers in polymer nanocomposites, Macromolecules 53 (2020) 2235–2248, https://doi.org/10.1021/acs.macromol.9b02429.